We are IntechOpen, the world's leading publisher of Open Access books Built by scientists, for scientists

6,900
Open access books available

185,000
International authors and editors

200M
Downloads

154
Countries delivered to

Our authors are among the

TOP 1%
most cited scientists

12.2%
Contributors from top 500 universities

CLARIVATE ANALYTICS
BOOK CITATION INDEX
INDEXED

WEB OF SCIENCE™

Selection of our books indexed in the Book Citation Index
in Web of Science™ Core Collection (BKCI)

Interested in publishing with us?
Contact book.department@intechopen.com

Numbers displayed above are based on latest data collected.
For more information visit www.intechopen.com

Chapter

Electrodeposition of High-Functional Metal Oxide on Noble Metal for MEMS Devices

Wan-Ting Chiu, Chun-Yi Chen, Tso-Fu Mark Chang, Tomoko Hashimoto and Hiromichi Kurosu

Abstract

MEMS gas sensors could exert a significant impact on the automotive sector since future legislation is expected to stipulate the monitoring of NO_x and unburned fuel gases in vehicle exhausts. Among the materials, zinc oxide and TiO_2 are the most promising and extensively used materials for monitoring of NO_x gas since zinc oxide and TiO_2 show the high sensitivity, good stability, and fast response. Electrochemistry is a potential method to fabricate zinc oxide and TiO_2 for the applications since it is carried out at relatively low temperature and can cooperate with photolithography, which is an important process in MEMS. This study integrated zinc oxide/gold-layered structure and TiO_2/NiP hybrid structure on elastic fabrics, respectively, to realize an elastic gas sensor. Electroless plating (EP) and cathodic deposition were used to metallize and deposit metal oxides on elastic fabrics. Supercritical carbon dioxide ($scCO_2$) was further introduced into the electrochemical process to enhance the composite reliability.

Keywords: MEMS gas sensors, zinc oxide, TiO_2, supercritical carbon dioxide, electroless plating

1. Introduction

The worldwide market of functional wearable devices (WD) is predicted to keep blossoming in the near future [1]. Meanwhile, WDs are differentiated into various functions such as gas sensor, and photocatalytic devices [2] due to different requirements in the next-generation technology. The combination of gas sensor materials and elastic substrate materials turns out to be the most crucial step in assembly of the component used in WDs. For instance, integration of gas sensor materials (i.e., zinc oxide and TiO_2), electrically conductive bases, and elastic substrate material is necessary to produce WDs-equipped gas sensing.

Elastic materials like cloth fabrics are mostly electrically insulator, and the elastic substrate material can be made electrically conductive by coating thin metallization layer on the electrically nonconductive substrate through electroless plating (EP) [3]. EP consists of a pretreatment procedure to clean the substrate material, a catalyzation (cat.) procedure to activate the substrate, and a metallization procedure to deposit metallization layer on the substrate material.

At (conventional) CONV cat. step, catalyst-included acidic aqueous solution is utilized to activate the substrate material by inlaying catalysts on substrates; meanwhile, the substrate morphology is often destroyed in this step. Due to polarity of the aqueous cat. solution and the high surface tension, the catalyst is merely deposited on the surface of the substrate bringing low adhesion between two materials. On the other hand, supercritical CO_2 ($scCO_2$) is introduced to the cat. procedure to improve the deposition characters [4, 5]. CO_2 turns into supercritical phase showing properties in the middle of gas phase and liquid phase as both the temperature and pressure are higher than its critical point [6]. $scCO_2$ is used as the solvent and a metal-organic complex was used as the catalyst. Due to the affinity to nonpolar material [7], low surface tension [8], and high self-diffusivity [6] of $scCO_2$, $scCO_2$ thus can convey the organic catalyst into confined spaces and carry it to go into the fabric while remains the substrate structure intact.

When it comes to the gas-sensing function, there are various fabrication methods to produce metal oxides (MO_x), which include high-temperature vapor deposition [9], polymer-mediated chemical reaction [10], hydrothermal-annealing procedure [11], and single-container electrolyte-based technique [12]. Among the fabrication techniques, cathodic deposition allows a facile and effective procedure for the fabrication of MO_x [13–16]. Furthermore, cathodic deposition can cooperate with lithography to allow further applications such as patterning, which is important for the MEMS fabrication process. The sensing material/metallization layer/elastic cloth fabric composite material was practiced by $scCO_2$-promoted EP and cathodic deposition toward applications in gas sensor in this study.

Even a slight uncomfortableness due to the rigid element in a WD can be annoying to the active users, and thus an elastic material is required in WDs. Silk fabric, a common clothing material, was selected due to its elasticity and stretchability in this study. A thin gold layer was selected as the electrically conductive layer. Furthermore, gold also shows great ductility [17], which is a critical prerequisite of WDs. There are many materials that can act as the sensing material in the hybrid material, such as titanium dioxide [18], copper (II) oxide [19], and zinc oxide [20]. Zinc oxide was deposited via cathodic deposition in this study as the sensing material due to its comprehensive applications, requirement of low fabrication temperature to have high crystallinity, and simple fabrication process.

On the other hand, co-EP technique was used in this study to equip the elastic silk fabric with electrically conductive NiP and sensing materials TiO_2 together by introducing TiO_2 particles into the NiP metallization electrolyte to form a suspension solution. Adhesive firmness can be enhanced by the included TiO_2 in the composite. There are several literature studied on the inclusion of TiO_2 in metal matrix via electrochemical methods such as electrodeposition and EP to enhance properties of the metal matrix. Gawad et al. [21] synthesized $NiP-Al_2O_3$ and $NiP-TiO_2$ composite layers on Cu substrate from alkaline hypophosphite gluconate baths and studied their properties. This study reported that inclusion of these oxide particles influences structure of the NiP matrix. Hardness, corrosion resistance, and coating brightness were enhanced with the TiO_2 inclusions. Thiemig and Bund [22] fabricated $Ni-TiO_2$ composite materials by electrocodeposition via an acidic sulfamate bath and an alkaline pyrophosphate electrolyte. Mechanical properties of the $Ni-TiO_2$ composite materials were enhanced while comparing to pure Ni electrodeposition in this literature. Parida et al. [23] investigated the ultrafine $Ni-TiO_2$ composite films by direct current electrodeposition technique on steel substrate from Watt's bath. With the inclusion of TiO_2 in the films, high microhardness and high wear resistance were realized while comparing to pure Ni electrodeposition. Benea et al. [24] worked on the electrocodeposition of Ni and TiO_2. The results showed high hardness and high wear resistance. Momenzadeh and Sanjabi [25]

studied the effect of TiO_2 concentration (conc.) in the electrolyte on the mechanical properties. They further introduced sodium dodecyl sulfate (SDS) surfactant into the electrolyte to increase the TiO_2 inclusion amount.

All the aforementioned literature worked on the mechanical properties such as wear resistance and hardness. In addition, all the composite materials were deposited on rigid substrates. However, flexibility is a critical requirement for gas sensing in WDs. There are merely limited literature working on decoration of metal-based composite on an elastic substrate and investigating its properties.

Here, we report a facile fabrication process in realization of an elastic and sensing material zinc oxide/gold/silk and TiO_2/NiP/silk-layered composite material, respectively, toward applications of gas sensor. Fundamental properties required for WDs such as electrical resistance, corrosion resistance, and adhesive firmness of the composite evaluations are demonstrated.

2. Silk/gold/zinc oxide hybrid structure

2.1 Activation of silk fabric via $scCO_2$ palladium (II) acetylacetonate cat.

Figure 1 shows OM images and X-ray diffraction patterns of the as-received silk and the catalyzed silk. The crossed-linked see-through bundles shown in **Figure 1(a)** imply the silk fabric, and the yellow flakes in **Figure 1(c)** specify the palladium (II) acetylacetonate catalyst. A broad peak at $2\theta = 20°$ can be observed in **Figure 1(b)**, which reveals an amorphous structure of the silk fabric. On the other hand, diffraction peaks labeled by diamond symbols can be corresponded to palladium (II) acetylacetonate [26, 27], and the results suggested the catalysts were successfully inlayed into the substrate. As shown in the OM figures, silk fabric persisted after the cat. procedure due to the low surface tension, low viscosity, and nonacidic characters of $scCO_2$. The $scCO_2$-promoted cat. step confirmed a significant enhancement while compare to the CONV cat. process. Palladium (II)
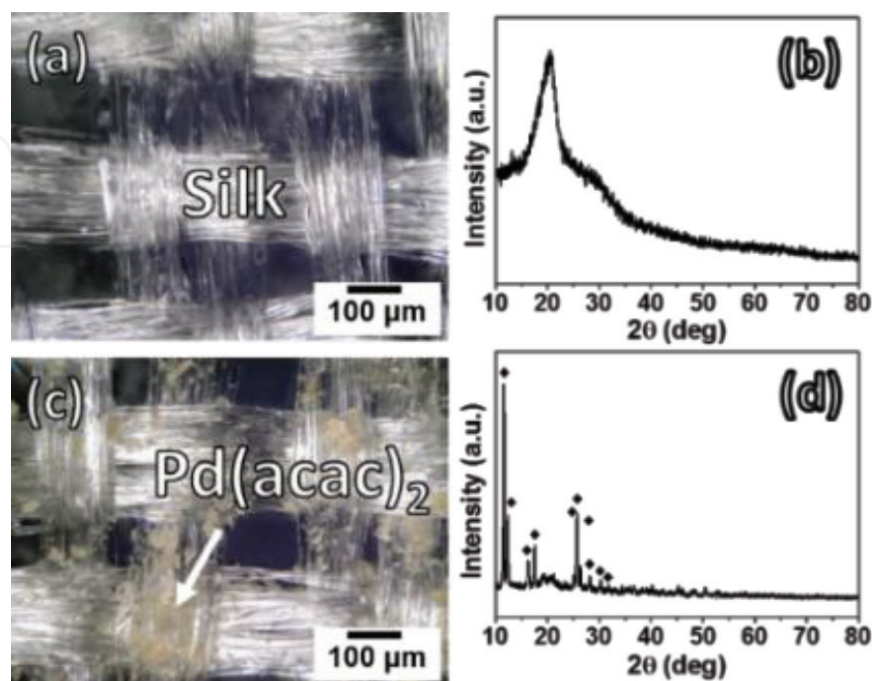

Figure 1.
(a) OM image and (b) X-ray diffraction pattern of the as-received silk as well as (c) OM image and (d) X-ray diffraction pattern of the catalyzed silk (diamond symbol: Pd(acac)₂ catalysts).

acetylacetonate acts as an activation site after it was reduced to Pd metal by the reductant in the metallization solution. Pd metal can play the role of catalyst and activate the following metallization.

2.2 Morphology, composition, and structure of silk/gold

Development of the gold layer is shown in **Figure 2**. **Figure 2(a)** shows morphology of the specimen with the NiP metallization period at 4 min before the gold metallization. **Figure 2(b–d)** demonstrates the gold metallization period at 3, 5, and 80 min, respectively. At 3 min of the gold metallization (**Figure 2(b)**), part of the NiP layer was still not enclosed showing a gray luster. As the gold metallization period was extended to 5 min and longer (**Figure 2(c)** and **(d)**), the NiP layer was completely concealed by the gold layer.

The X-ray diffraction patterns at various gold metallization periods are shown in **Figure 3(a–c)**. Five apparent diffraction peaks shown in **Figure 3(a–c)** locate at $2\theta = 38.2, 44.4, 64.6, 77.6$, and $81.7°$ can be indexed to (111), (200), (220), (311), and (222) planes, respectively, of the FCC structure for gold (JCPDS #65-2870). In **Figure 3(a)**, at 3 min of the gold metallization period, only a thin layer of gold was metallized on the silk, and the broad diffraction peak of silk at around 20° was still detectable. NiP diffraction peaks were not found in **Figure 3(a)**, because the NiP metallization layer is selected as the sacrificial metallization layer for thin gold metallization. Moreover, it performs amorphous structure, which the amorphous peaks are overlaid by the gold diffraction peaks with high intensity. As the gold metallization continued, no diffraction peaks of the silk fabric were detected in the X-ray diffraction patterns (**Figure 3(b** and **c)**) since the gold layer is thick enough to suppress the diffraction peaks from the silk. **Figure 3(d)** indicates the composition change with the gold metallization period. In the first place, owing to the inadequate thickness of gold, the thin NiP metallization layer was detected by EDX. On the other hand, thin NiP metallization layer was no longer found when the gold metallization period extended to 80 min. Phosphorus was not found due to the inadequate quantity.
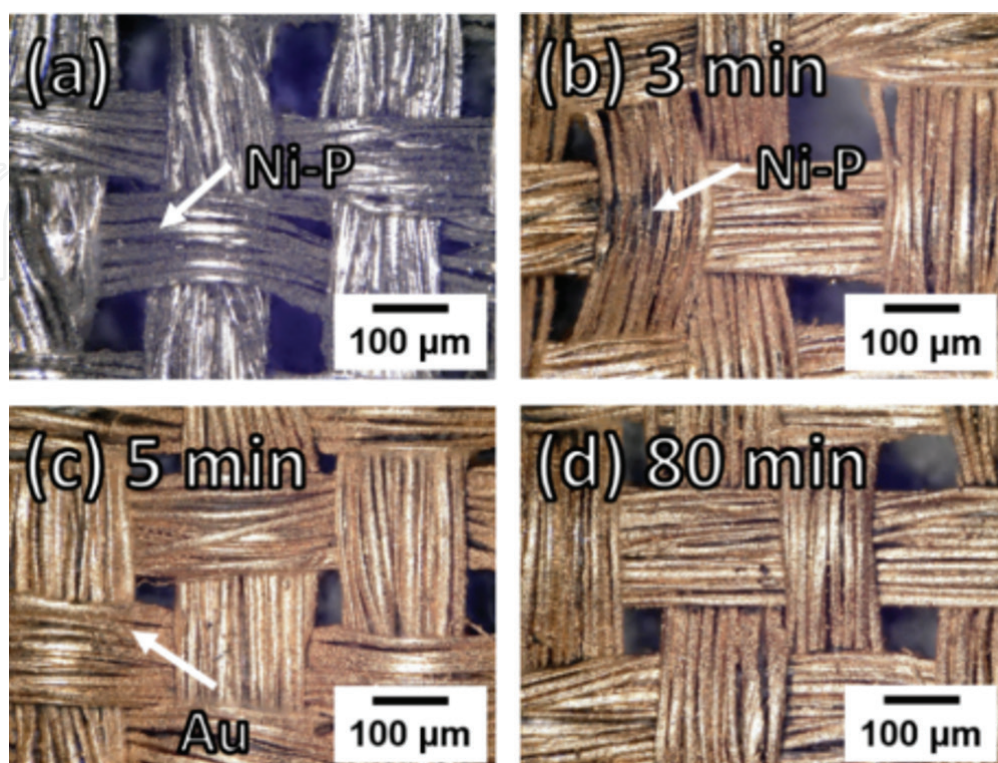

Figure 2.
OM images of the (a) Ni-P metallized silk and the Au metallization at (b) 3 min, (c) 20 min, and (d) 80 min.
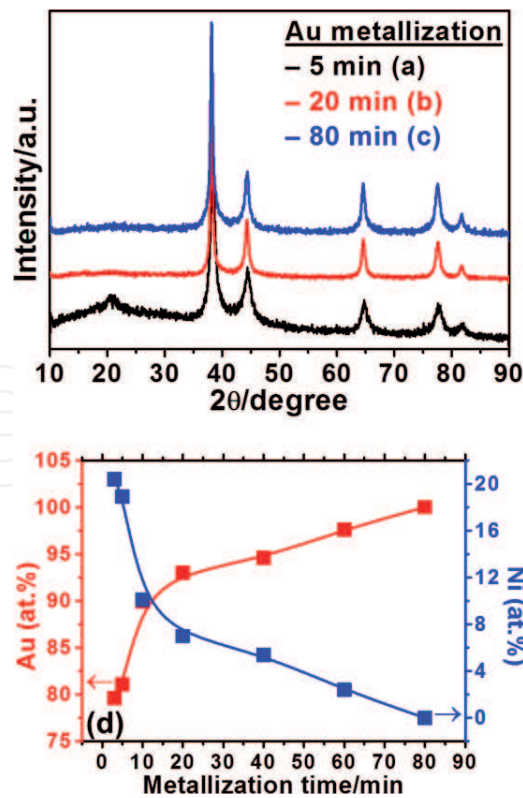
Figure 3.
X-ray diffraction patterns of the Au metallization at (a) 5 min, (b) 20 min, and (c) 80 min and (d) the composition revolution with the Au metallization time.

Figure 4 illustrates growth of the gold layer thickness with the gold metallization period. There is no obvious partition of the NiP and gold layer shown in the inserted SEM image in **Figure 4**. A positive interrelationship was observed between thin gold metallization layer and the gold thickness showing the growth rate in average at 0.48 μm/h. The growth rate decreased marginally from 60 to 80 min of the gold metallization period due to the consumption and decline in concentration of the metal ion and reductant as the deposition continued.
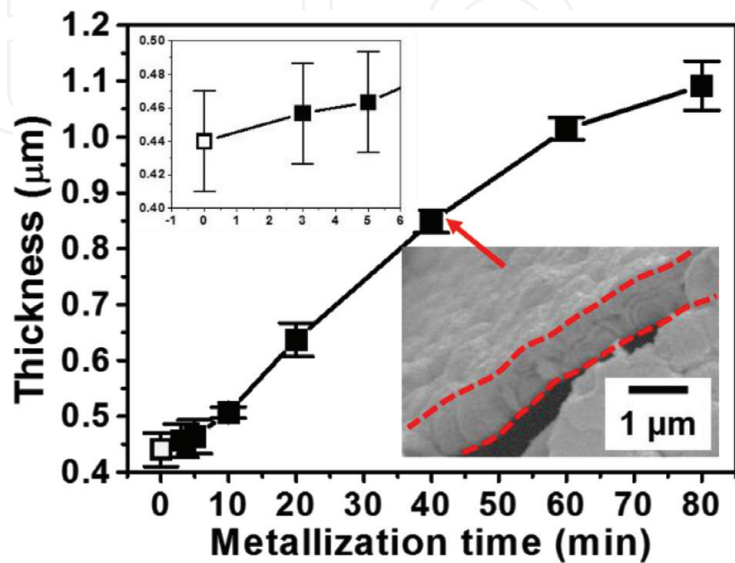

Figure 4.
Plot of the Au metallization thickness versus the metallization time (hollow symbol: NiP metallization at 4 min and solid symbols: Au metallization thickness versus Au metallization time) (OM image of Au metallized at 40 min of the metallization time is inserted into bottom-right).

2.3 Electrical property of silk/gold

The electrical resistances at various gold metallization periods are shown in **Figure 5**. The electrical resistance dropped down in the early stage and increased after reaching a minimum point. Since the NiP layer is not fully covered by gold at 3 min of gold metallization period (solid symbol) (**Figure 2(a)**), it showed high electrical resistance close to the gold-free specimen at 0 min of gold metallization (hollow symbols) (**Figure5(a)**). An inserted graph in **Figure 5(a)** shows results of the gold metallization period between 0 and 5 min.

The electrical resistances obtained from 0 to 5 min (the dash line shown in **Figure 5**) of the metallization period, which only showed a minor difference from the gold-free one, are categorized into the first stage. Full coverage was built as the gold metallization period reached 5 min, and the electrical resistance was enhanced consequently. The electrical resistance reached its minimum at the gold metallization period of 20 min due to the full coverage, smooth deposition, and adequate gold thickness (**Figure 5(b)**). From the beginning of the full coverage to the range near the lowest electrical resistance can be classified to the second stage (from the dash line at 5 min to the other one at 40 min). The electrical resistance increased marginally as the gold metallization period increased beyond the minimum point. The surface became rougher (indicated by the arrows in **Figure 5(c)**) with the lengthened metallization period, and the electrical resistances were worsened due to more scattering of electrons [28]. The section of deteriorated electrical resistance and rough deposition can be characterized into the third stage.
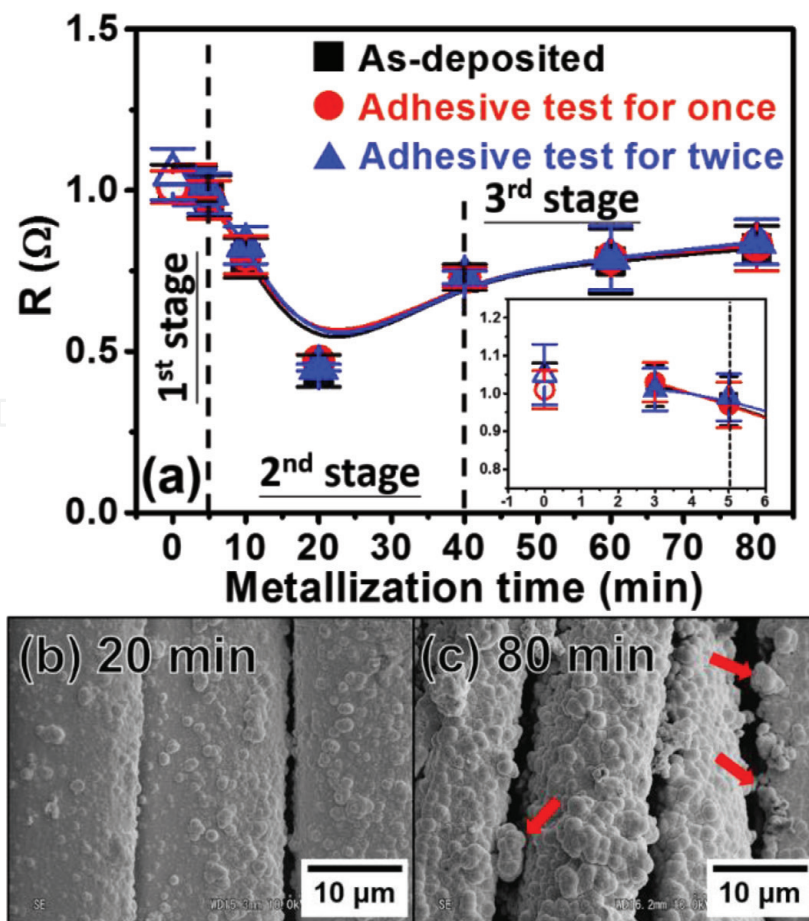

Figure 5.
(a) Electrical resistances of the Au-metallized silk at various metallization times and SEM images of the Au-metallized silk at (b) 20 min and (c) 80 min of the metallization time (hollow symbols: Au-free; solid symbols: Au metallized).

The electrical resistances with the adhesive treatments are also shown in **Figure 5(a)**. No substantial change was found in all stages because silk fabric was entirely deposited by the NiP and gold, and the adhesive property between the silk fabric and the NiP as well as between the NiP and the gold metallization layer both showed high adhesion.

2.4 Cathodic zinc oxide fabrication

Figure 6 shows SEM images (**Figure 6(a–d)**) and OM images (**Figure 6(e–h)**) of the pristine zinc oxide deposited with hydrogen peroxide concentration varied from 0 to 0.3 wt.%. Tower-like zinc oxide nanowires are observed in all of the SEM images (**Figure 6(a–d)**). Zinc oxide coverage on the gold metallization layer was conducted and calculated by a built-in software in OM. Zinc oxide coverages were at 63, 62, 41, and 32% for the samples fabricated with free hydrogen peroxide to 0.3 wt.% hydrogen peroxide. Structure of zinc oxide is often influenced by chloride ion in the electrolyte. The chloride ion acts as a capping agent adsorbing on the
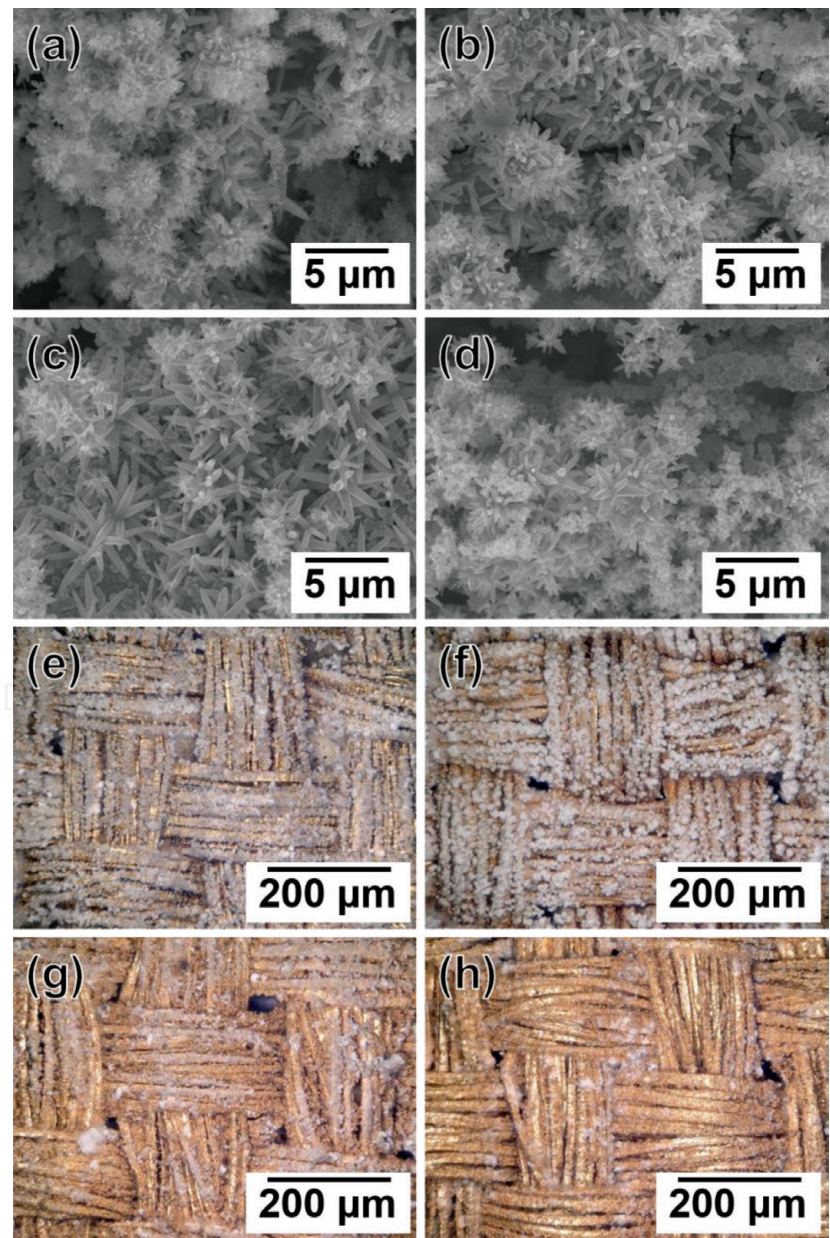

Figure 6.
SEM images of the specimens deposited in (a) free of H_2O_2, (b) 0.1 wt.%, (c) 0.2 wt.%, and (d) 0.3 wt.% H_2O_2, and the OM images in (e) free of H_2O_2, (f) 0.1 wt.%, (g) 0.2 wt.%, and (h) 0.3 wt.% H_2O_2.

(0001) plan of zinc oxide to stabilize zinc oxide surface and results in development of nanorod-like morphologies. In contrast, when concentration of the chloride ion is low, tower-like morphologies rather than nanorod morphologies are developed [29]. Moreover, zinc oxide particle size increased as the hydrogen peroxide concentration increased from 0 to 0.2 wt.% as shown in the SEM images. Similar results on increase in the zinc oxide particle size as the hydrogen peroxide concentration increased were stated in a literature [30]. However, in **Figure 6(d)**, the particle size decreased when the hydrogen peroxide concentration went beyond 0.2 wt.%. Zinc oxide cathodic deposition reaction equations are as follows [31]:

$$NO_3^- + H_2O + 2e^- = NO_2^- + 2OH^- \tag{1}$$

$$H_2O_2 + 2e^- = 2OH^- \tag{2}$$

$$Zn^{2+} + 2OH^- = ZnO + H_2O \tag{3}$$
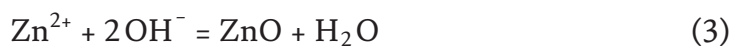
OH$^-$ formed on the electrode from Eqs. (1) and (2) is predicted to react with zinc ion in the solution to form zinc oxide on the electrode. As shown in Eq. (2), formation rate of the hydroxide ion is increased with high hydrogen peroxide concentration. Since the diffusivity of zinc ion in aqueous electrolyte is four times slower than that of hydrogen peroxide, zinc ion diffusion to the electrode surface cannot catch up with the formation of hydroxide ion as the hydrogen peroxide concentration increased [32]. As the amount of hydrogen peroxide was increased to 0.3 wt.%, formation rate of the hydroxide ion is too high and accumulates at the substrate surface.

A general scheme of the solute concentration profiles in the solution is shown in **Figure 7**. Hydroxide ions are formed on the electrode; hence, the concentration is progressively lowered toward the bulk electrolyte direction. Zinc ions diffuse from the bulk electrolyte to the electrode surface to react with hydroxide ions; therefore, the concentration decreases as it approaches the electrode surface. Depending on the hydroxide ion formation rate, local hydroxide ion concentration, or pH, on the electrode varies. Zinc oxide is deposited at a pH range of ca. 8–12, and zinc oxide dissolves away to form ZnO_2^{2-} or $HZnO^{2-}$ as the pH goes beyond 12 [33, 34]. The region appropriate for the formation of zinc oxide is defined as region I, and the region results in dissolution of zinc oxide is classified as region II as shown in **Figure 7**.

The range near surface of the electrode is in region I when the hydrogen peroxide concentration was lower than 0.2 wt.%. Hence, an increase in the hydrogen peroxide concentration resulted in particle size increase (**Figure 6(a** and **b)**) and the high coverage (**Figure 6(e** and **f)**). As the hydrogen peroxide concentration was increased to 0.3 wt.%, both the zinc oxide particle size (**Figure 6(d)**) and the coverage (**Figure 6(h)**) were declined, which indicates the pH near electrode surface could be higher than 12. The results suggest the region near the electrode surface is in region II as the hydrogen peroxide concentration is higher than 0.3 wt.%.

Figure 8(a) shows X-ray diffraction patterns of the zinc oxide deposited with various hydrogen peroxide concentrations in the electrolyte. Only the diffraction peaks of gold (star symbol) and zinc oxide (hexagon symbol) were observed. No other phase was found in the X-ray diffraction patterns after the zinc oxide deposition. A comparative crystallinity of zinc oxide on the gold metallization was approximately estimated by calculating ratio of the gold (111) intensity to the zinc oxide (100) intensity with consideration of the zinc oxide coverage. The ratios were at 0.10, 0.11, 0.34, and 0.16 from free of hydrogen peroxide to 0.3 wt.% hydrogen
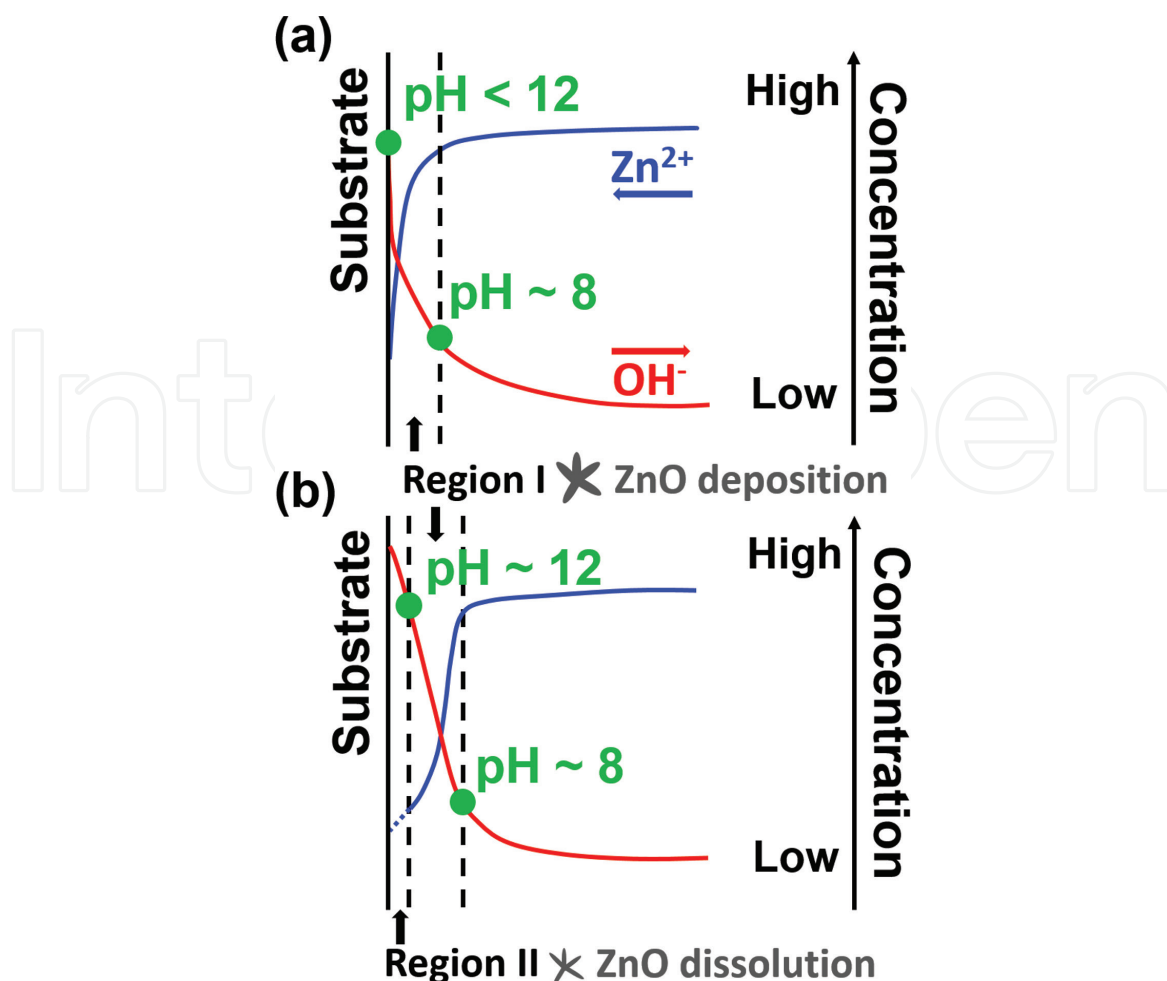
Figure 7.
General scheme of the solute concentration profiles: (a) low OH⁻ concentration and (b) high OH⁻ concentration.

peroxide. The ratios suggested the solution containing 0.2 wt.% hydrogen peroxide deposited zinc oxide with the highest crystallinity, and the crystallinity became inferior when 0.3 wt.% hydrogen peroxide was used. Another explanation regarding to crystallinity of the zinc oxide is elaborated here. Crystallinity of the zinc oxide is known to be dependent on concentration of the zinc ion [35], which defects and worsened crystallinity are introduced to the zinc oxide when the zinc ion concentration is lowered. In this study, as the hydrogen peroxide concentration reached 0.3 wt.%, local concentration of hydroxide ion near the substrate surface is high, and high diffusion rate of hydroxide ion to the bulk electrolyte was constructed. Then, pH far away from the electrode surface became appropriate for deposition of zinc oxide and consumed high amount of the zinc ion. In this case, amount of the zinc ion diffused to the electrode surface was lowered and brought the low crystallinity.

Figure 8(b) shows the voltage-time plot in the zinc oxide cathodic deposition. When there is hydrogen peroxide in the solution, potential drop diminished as the hydrogen peroxide concentration increased. The potential drop here refers to the potential difference between the potential at ca. 0 s of the reaction time and the potential as the reaction steadily stabilized with deposition time. No obvious difference was detected in the specimens cathodically deposited with free of hydrogen peroxide and 0.1 wt.% hydrogen peroxide, which are in good agreement with the zinc oxide coverage in **Figure 6(e)** and **(f)** indicating that 0.1 wt.% hydrogen peroxide has only limited effect on the zinc oxide cathodic deposition. The potential oscillation became obvious with hydrogen peroxide concentration, which is because more N_2 gas is produced at high pH [36].
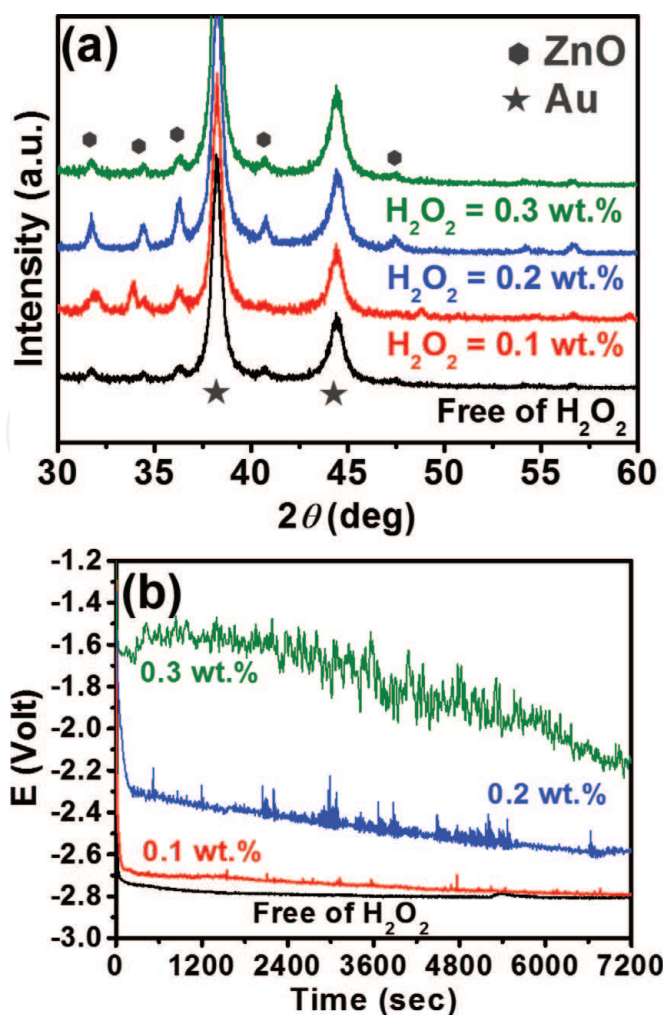
Figure 8.
(a) X-ray diffraction patterns and (b) voltage-time plot of the specimens fabricated with electrolytes containing various H_2O_2 concentrations.

3. Silk/NiP/TiO$_2$ hybrid structure

3.1 Activation of silk fabric via scCO$_2$ palladium (II) acetylacetonate cat.

Figure 9 shows OM images and XRD patterns of the as-received silk and the scCO$_2$-catalyzed silk. The transparent interwoven bundles shown in **Figure 9(a)** indicate the silk fabric, and **Figure 9(b)** shows a broad peak at around $2\theta = 20°$; this broad peak reveals an amorphous structure of the silk fabric. The light yellow flakes around the silk bundles in **Figure 9(c)** specify the palladium (II) acetylacetonate, and the diffraction peaks in **Figure 9(d)** labeled by triangle symbols can be indexed to palladium (II) acetylacetonate very well [26, 27], which indicated that the palladium (II) acetylacetonate organometallic compounds were successfully deposited on the silk substrate. As demonstrated in the **Figure 9(a)** and **(c)**, the silk fabric remained undamaged after the 2 h scCO$_2$ cat. treatment due to the low surface tension, low viscosity, and noncorrosive properties to most of polymers of scCO$_2$ [37–39]. The scCO$_2$ cat. practiced a significant advancement when it is compared to the CONV cat. process [37].

3.2 NiP/TiO$_2$ codeposition

Surface conditions of the NiP/TiO$_2$-decorated silk fabrics prepared from the NiP electrolytes containing various TiO$_2$ concentrations (0, 10, 20, 30, 40, and 50 g/L) can
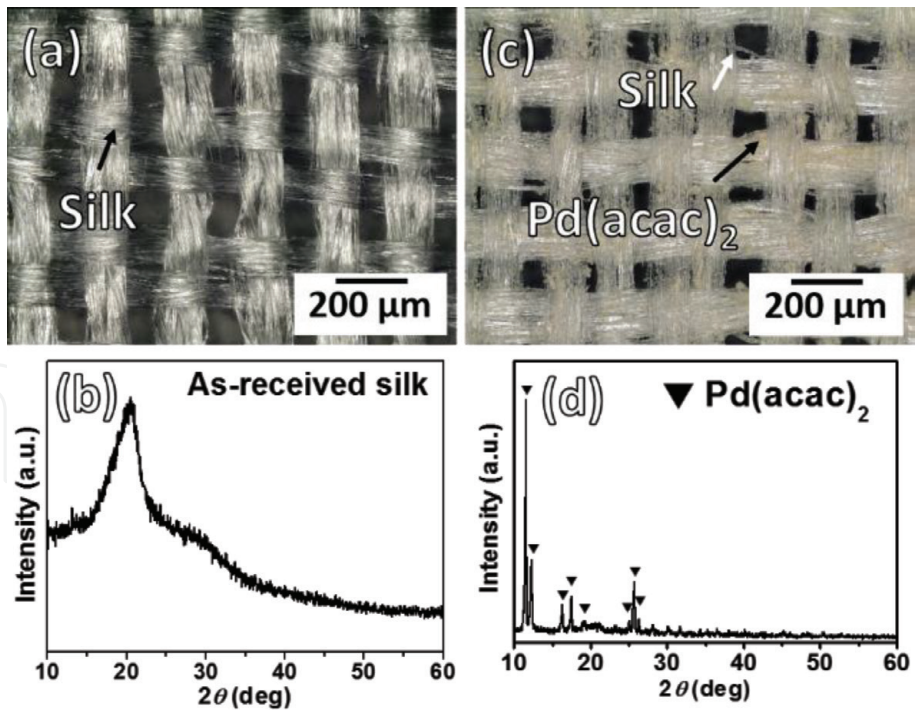
Figure 9.
(a) OM image and (b) XRD pattern of the as-received silk, and (c) OM image and (d) XRD pattern of the scCO₂ catalyzed silk (triangle symbols: Pd(acac)₂).

be observed from SEM and OM images (inserted into top-left of each SEM images) shown in **Figure 10**. **Figure 10(a)** shows morphology of the specimen deposited without TiO$_2$ particles in the NiP electrolyte. It shows smooth surface while comparing to the other ones deposited with TiO$_2$ in the electrolyte (**Figure 10(b–f)**). The bright nano-sized protrusions shown in **Figure 10(b–f)** indicate the deposition of
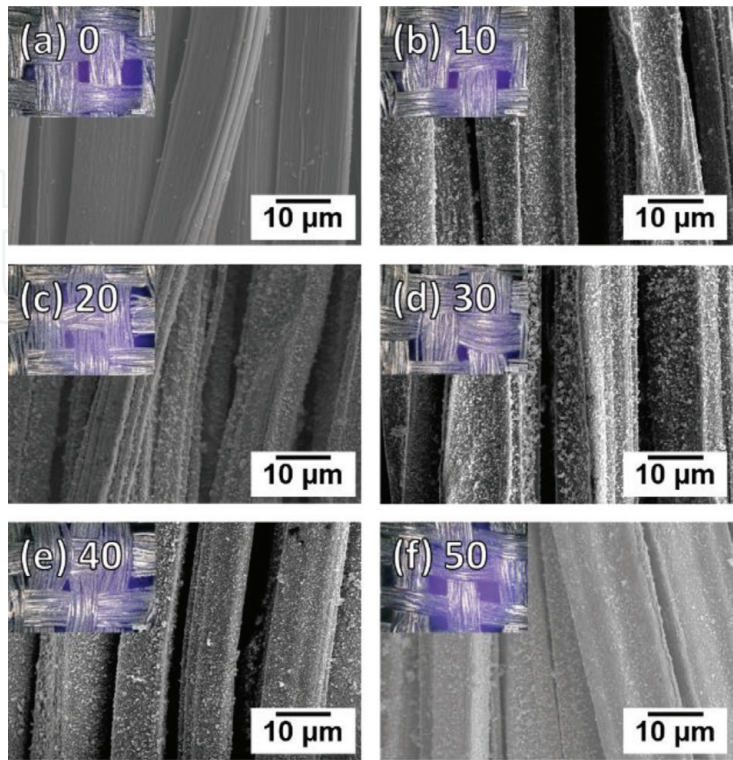

Figure 10.
SEM images and OM images (inserted into top-left) of NiP/TiO₂ deposition with various TiO₂ concentrations at (a) 0, (b) 10, (c) 20, (d) 30, (e) 40, and (f) 50 g/L, respectively.

TiO$_2$ which resulted in roughening of the surface. However, the surface roughness decreased when the TiO$_2$ concentration went beyond 30 g/L in NiP electrolyte.

The nanoscale TiO$_2$ particles in the electrolyte would aggregate to form large aggregate particles, and average size and size distribution of the aggregate particle are related to concentration of the oxide particles in the solution [40–45]. In this study, when the TiO$_2$ concentration is low (10 and 20 g/L), there is only slight aggregation of the TiO$_2$ particles in the NiP electrolyte. Average size of the aggregate particle size is small, and the distribution is narrow as illustrated in **Figure 11(a)**. Level of the aggregation gradually increases with an increase in concentration of the TiO$_2$, and average size of the aggregate particle becomes larger with a wider size distribution as shown in **Figure 11(b and c)**. Compositions of NiP/TiO$_2$ depositions are shown in **Table 1**.

The mechanism of the TiO$_2$ inclusion is illustrated in **Figure 12**. It is suggested that Ni ions would adsorb on surface of the TiO$_2$ aggregate particles suspending in the electrolyte to form Ni^{2+}-TiO$_2$ complex particles, and the complex particles diffuse to the substrate; then, reduction of the Ni ions on surface of the complex particle occurred to engulf the TiO$_2$ aggregate particle into the NiP layer [24, 26]. When the TiO$_2$ concentration is low with a small aggregate particle size in the electrolyte, the TiO$_2$ aggregate particles are easily included into the NiP as shown in **Figures 11(a)** and **12(a)**. Because of the small aggregate particle size, a relatively smooth surface is obtained as exampled by the specimen shown in **Figure 10(b and c)**. With an increase in the TiO$_2$ concentration, average size of aggregate particles included into the NiP gradually increases and leads to a roughened surface condition as illustrated in **Figure 12(b)**. **Figure 10(d)** demonstrates the result of the rough surface caused by the large aggregate particles in the moderate aggregate region (**Figure 11(b)**). The largest TiO$_2$ aggregate particle size was found at approximate 0.7 μm. When size of the TiO$_2$ aggregate (or the Ni^{2+}-TiO$_2$ complex) particle reaches a critical size, a phenomenon named steric obstruction takes place to affect inclusion of the particles [46–53]. Steric obstruction is unfavorable for the inclusion as shown in **Figure 12(c)**. At first, removal of already-adsorbed oxide
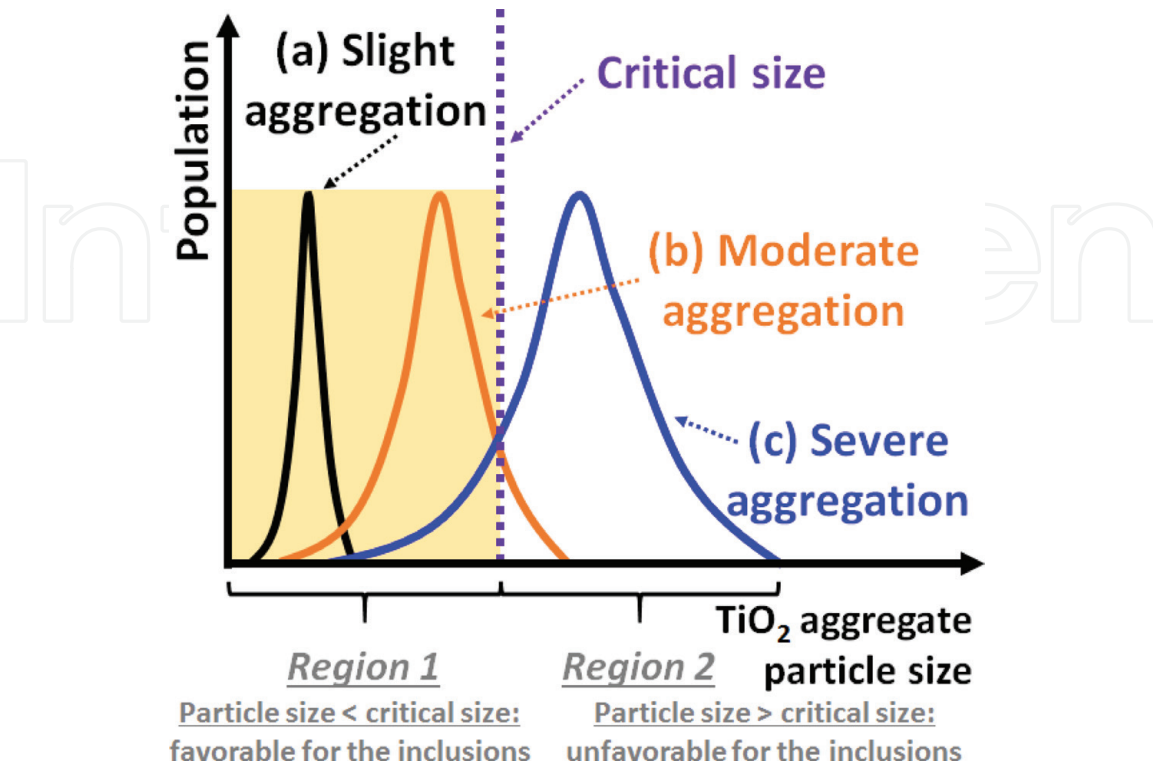

Figure 11.
TiO$_2$ particle size distribution with different amount of TiO$_2$ in the electrolyte: (a) slight aggregation, (b) moderate aggregation, and (c) severe aggregation.

Atom	TiO₂ (g/L)						
	0	10	20	30	40	50	60
P (at.%)	22.11	18.82	19.85	19.89	19.17	18.37	20.09
Ti (at.%)	0.00	4.62	5.95	10.16	6.15	5.32	4.76
Ni (at.%)	77.89	76.56	74.20	69.95	74.68	76.31	75.15
Sum	100.00	100.00	100.00	100.00	100.00	100.00	100.00

Table 1.
Composition of as-deposited NiP/TiO₂ metallization layers on silk textiles.
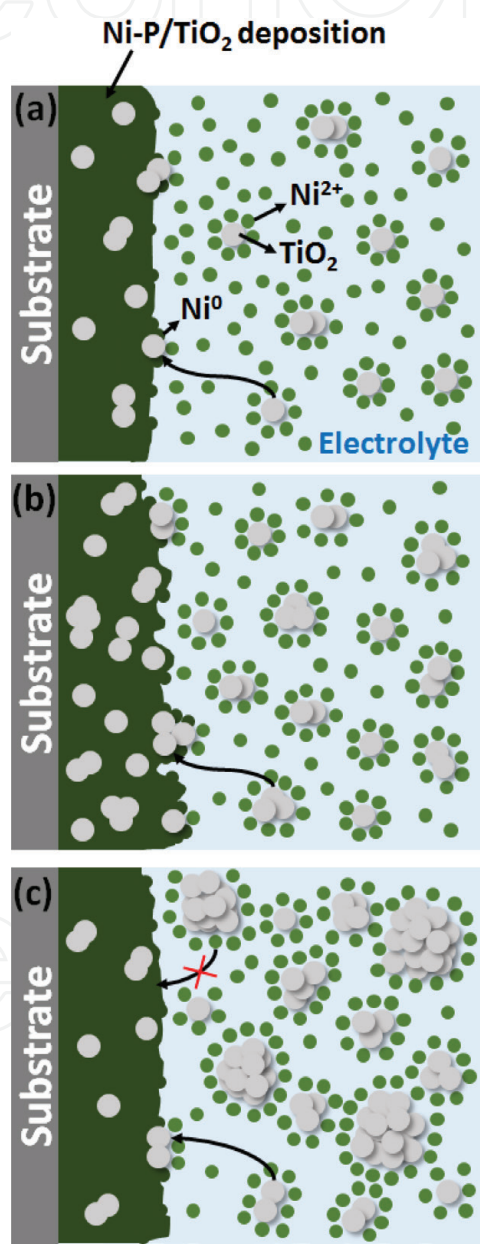

Figure 12.
Mechanism of TiO₂ inclusion with (a) TiO₂ concentration less than critical amount, (b) TiO₂ concentration at critical amount, and (c) TiO₂ concentration more than critical amount.

particles and decrease in the number of new particles adhering to the substrate occur because of collisions between particles near the substrate [54]. Secondly, inclusion of the particles is dependent on reduction of Ni ions adsorbed on the aggregate TiO₂ particle surface. Surface-to-volume ratio of the aggregate particle is lowered with an increase in the aggregate TiO₂ particle size. When the aggregate TiO₂ particle size is

larger than the critical size, shortage of Ni ions adsorbed on surface of the particle makes it less likely to include the aggregate TiO_2 particle into the NiP before been removed away from the surface because of the collision [55]. In this study, average size of the aggregate TiO_2 particle is suggested to be close to the critical size causing the steric obstruction when the TiO_2 concentration is at 30 g/L (**Figures 10(d)** and **12(b)**), which is defined as the critical concentration resulting either maximum or minimum characteristics in the composite.

Figure 13 shows elemental mapping results of the NiP/TiO_2 composite prepared with the electrolyte containing 30 g/L of TiO_2. **Figure 13(a)** shows the rough surface condition of the composite layer deposited at the critical concentration. P, Ni, and Ti elements were homogeneously distributed on the surface indicating well-mixing of the electrolyte and homogeneous distribution of TiO_2 in the composite layer as indicated by results shown in **Figure 13(b)–(d)**. The compositions of NiP/TiO_2 are shown in **Table 1**.

Figure 14 shows XRD patterns of the NiP/TiO_2-deposited silk fabrics at various TiO_2 concentrations in the electrolyte. A broad peak at around $2\theta = 45°$ indicates amorphous structure of the NiP phase, while a sharp peak at around $2\theta = 25°$ suggests anatase phase of the TiO_2. All specimens show TiO_2 diffraction peak at $2\theta = 25°$ except for the one without the introduction of TiO_2 (0 g/L) in **Figure 14(a)**. No impurity or third phase was found in the XRD pattern within the detection limitation. TiO_2 concentration was approximately compared by the ratio between intensities of the NiP and the TiO_2 major peaks to qualitatively estimate the TiO_2 concentration in the NiP metallization layer. The ratio increased as concentration of TiO_2 in the electrolyte increased until it reached 30 g/L, which implies an increase in concentration of TiO_2 in the composite layer. Then, the ratio decreased indicating a decrease in concentration of TiO_2 in the composite layer (**Figure 14e** and **f**). This observation confirmed 30 g/L of TiO_2 in the electrolyte being the critical concentration to give the highest TiO_2 inclusion in the composite and the effect of steric obstruction (**Figures 11** and **12**).

Figure 15 illustrates a positive correlation between the NiP/TiO_2 composite layer thickness and the TiO_2 concentration in the electrolyte before reaching the critical concentration. A SEM image was inserted in the bottom-right corner of **Figure 15** to show cross-section of the silk/NiP/TiO_2 composite layer deposited with 50 g/L TiO_2 in the electrolyte. The average growth rate was at 3.4 μm/h before reaching the
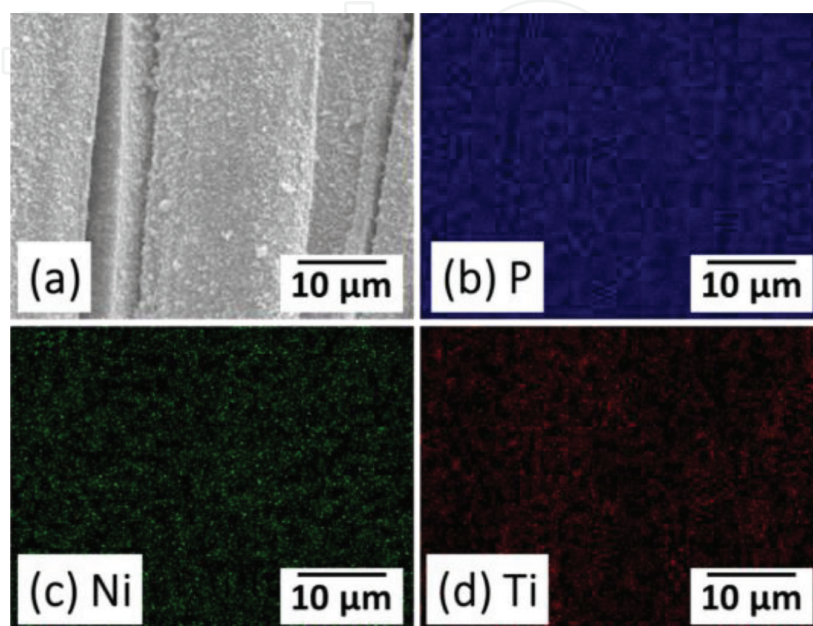

Figure 13.
Elemental mapping of NiP/TiO₂ composite layer deposited with 30 g/L TiO₂.
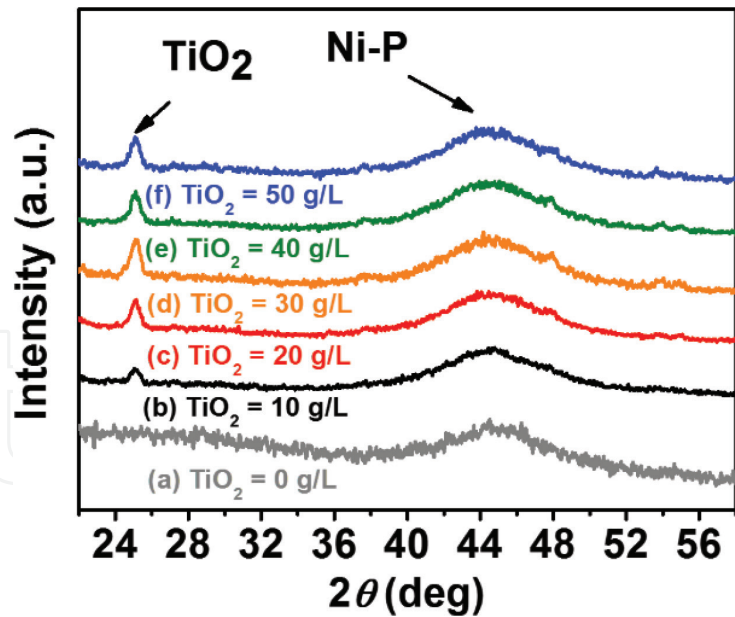
Figure 14.
X-ray diffraction patterns of NiP/TiO₂ deposition with various TiO₂ concentrations at (a) 0, (b) 10, (c) 20, (d) 30, (e) 40, and (f) 50 g/L, respectively.

critical concentration. On the other hand, the thickness decreased slightly in the 40 and 50 g/L specimens since large TiO_2 aggregate particles were formed to cause the steric obstruction (**Figures 11** and **12**).

3.3 Electrical conductivity and adhesive tests

Electrical resistances of composite layers prepared at various TiO_2 concentrations in the NiP electrolyte are shown in **Figure 16**. Since TiO_2 is a semiconductor, it owns lower electrical conductivity than NiP. TiO_2 thus shows negative influence on the electrical conductivity in the NiP metallization layer. NiP metallization layer without TiO_2 inclusion performed the lowest electrical resistance. The electrical resistance increased monotonously with TiO_2 concentration in the electrolyte before reaching the critical concentration of TiO_2 (30 g/L) in the electrolyte. On the other hand, when the TiO_2 concentration in the electrolyte went beyond the critical concentration, the electrical resistance dropped owing to lower TiO_2 concentration in the NiP metallization layer. The inclusion trend of TiO_2 revealed by the electrical
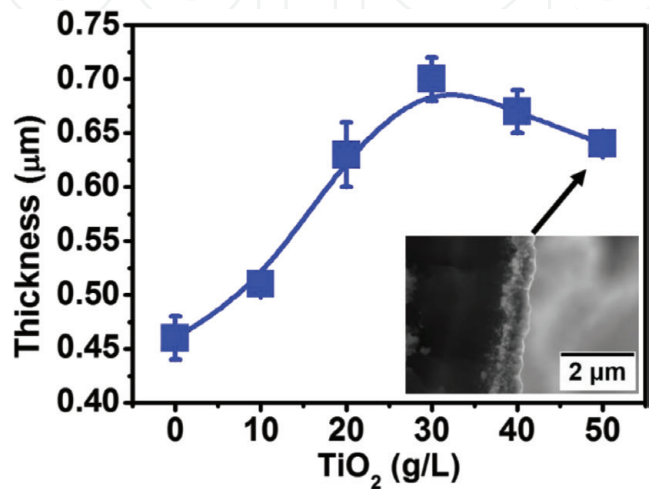

Figure 15.
Relationship of NiP/TiO₂ thickness and TiO₂ concentration in the electrolyte.
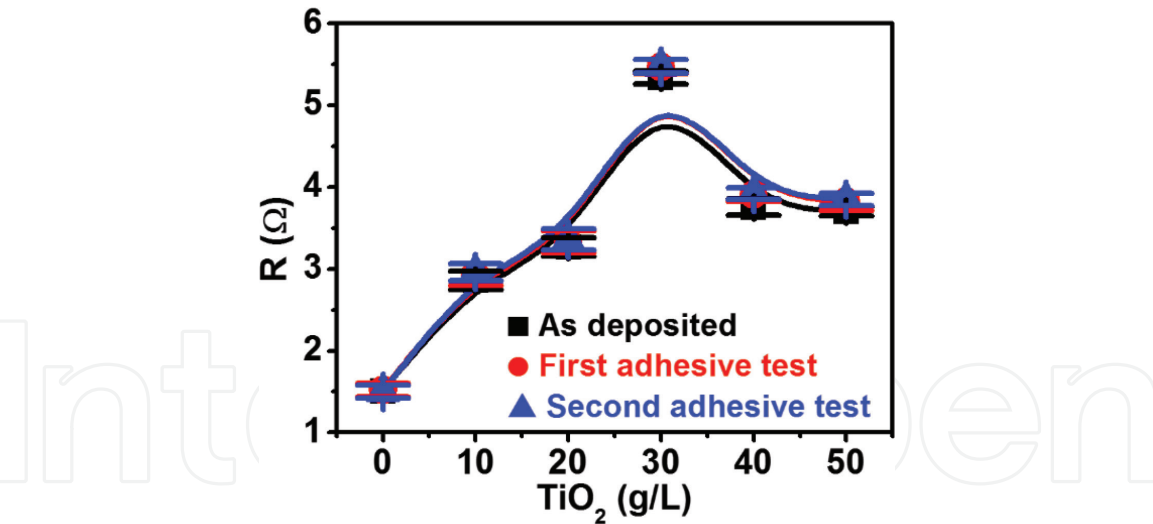
Figure 16.
The influence of included TiO₂ concentration to the electrical resistance of the silk/NiP/TiO₂ composite material.

resistances is in accordance with the surface morphologies from SEM observations, the intensity ratios from XRD patterns, and the layer thickness results.

Adhesive test evaluations are also shown in **Figure 16**. Square symbol represents the as-deposited specimen, circle symbol depicts the first adhesive test, and the triangle one indicates the second adhesive test. Here, first adhesive test indicates one
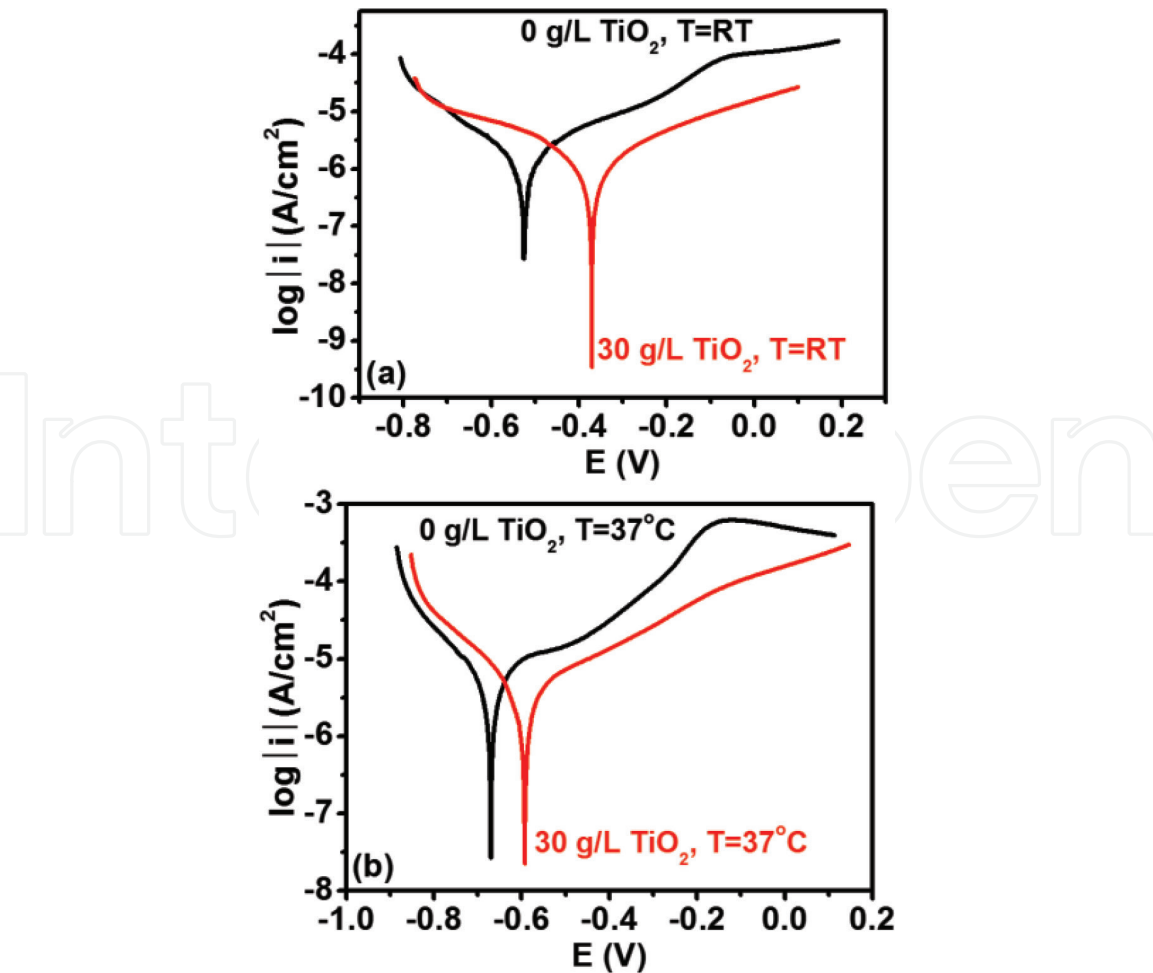

Figure 17.
Polarization curves of pure NiP coating and NiP/TiO₂ (3 g/L TiO₂ in the electrolyte) deposition on silk textile at (a) room temperature and (b) 37°C (body temperature).

	E_{corr} (V)	I_{corr} (A/cm^2)
(a) Room temperature		
Silk/NiP	−0.53	6.00×10^{-7}
Silk/NiP/TiO$_2$ (3 g/L)	−0.37	1.56×10^{-7}
(b) 37°C (body temperature)		
Silk/NiP	−0.67	3.79×10^{-6}
Silk/NiP/TiO$_2$ (3 g/L)	−0.59	1.02×10^{-6}

Table 2.
Corrosion potentials and corrosion current densities of the silk/NiP and silk/NiP/TiO$_2$ composites in 3.5 wt.% NaCl at (a) room temperature and (b) 37°C (body temperature).

cycle of the adhesive treatment is performed. Accordingly, second adhesive test means two cycles of the test are conducted. The results show that the electrical resistances persisted after the second adhesive test. Moreover, no significant difference was found between the first and second adhesive tests, and thus no further adhesive tests were conducted. These results demonstrate the high reliability and the robustness of the silk/NiP/TiO$_2$ composite materials and indicate that it is practicable for WDs.

3.4 Corrosion resistance

Figure 17 shows the corrosion behaviors of the as-deposited silk/NiP composite and the silk/NiP/TiO$_2$ composite materials in 3.5 wt.% NaCl solution at both room temperature (**Figure 17(a)**) and 37°C (body temperature) (**Figure 17(b)**). The silk/NiP/TiO$_2$ composite fabricated with 30 g/L of TiO$_2$ in the electrolyte was chosen for the corrosion resistance evaluations. The corrosion potential (E_{corr}) and the corrosion current density (j_{corr}) are summarized in **Table 2**. These results show that the NiP/TiO$_2$ composites have excellent corrosion resistance when compared with the pure NiP coating at both room temperature and 37°C. According to the results, TiO$_2$ particles play an important role for the improvement of the corrosion resistance. TiO$_2$ particles act as inert physical barriers to the initiation and development of defect corrosion and modify microstructure of the NiP metallization layer to improve the corrosion resistance. On the other hand, the E_{corr} of silk/NiP/TiO$_2$ is more positive than the silk/NiP indicating that the silk/NiP/TiO$_2$ composite is more inert than the silk/NiP due to the inclusion of inert TiO$_2$ particles. This result demonstrates that the composite material can persist in salty human sweat at both room temperature and body temperature, which is promising for applications toward WDs.

4. Conclusions

Zinc oxide/gold-layered structure was successfully integrated on the silk fabric by scCO$_2$-promoted EP and cathodic deposition. Conventional problems encountered in the CONV EP were solved by the scCO$_2$-promoted technique. By the introduction of scCO$_2$, silk fabric was catalyzed without damages and the adhesion between silk fabric and the metallization layer was improved in the meanwhile. Surface coverage and thickness of gold metallization layer increased with the gold metallization period. The lowest electrical resistance was realized as the gold metallization period lengthened to 20 min. On the other hand, zinc oxide was fabricated on the gold-metallized silk fabric via the cathodic deposition technique. The depositions on the silk fabric have been detected to be metallic gold phase and zinc oxide wurtzite phase. Zinc

oxide deposited with 0.2 wt.% hydrogen peroxide performs the highest crystallinity showing the best photocurrent density. The zinc oxide-decorated specimen with 0.2 wt.% hydrogen peroxide performed 11.5 times improvement in the photocurrent density while compares to that of hydrogen peroxide-free one.

NiP/TiO_2 composite layer was successfully codeposited on silk fabric by $scCO_2$-assisted EP. Common difficulties encountered in the CONV EP were solved by the introduction of $scCO_2$, and the palladium (II) acetylacetonate organometallic compounds were embedded into the silk substrate. The composite layer on the silk was confirmed to be amorphous NiP phase and TiO_2 anatase phase. The composite showed the highest electrical resistance when the concentration of TiO_2 in the electrolyte was 30 g/L (critical concentration) since the highest TiO_2 concentration was included into the Ni-metallization layer. The largest TiO_2 aggregate particle size was found approximate 0.7 μm at the critical concentration. Highly adhesive property of this silk/NiP/TiO_2 composite was revealed by the adhesive tests and the electrical resistance. The NiP/TiO_2 showed higher corrosion resistance than that of NiP-metallized silk without TiO_2 particles at both room temperature and body temperature.

Acknowledgements

Conflict of interest

We have no conflict of interest to declare.

Author details

Wan-Ting Chiu[1]*, Chun-Yi Chen[1], Tso-Fu Mark Chang[1], Tomoko Hashimoto[2] and Hiromichi Kurosu[2]

1 Institute of Innovative Research, Tokyo Institute of Technology, Yokohama, Japan

2 Department of Clothing Environmental Science, Nara Women's University, Nara, Japan

*Address all correspondence to: chiu.w.aa@m.titech.ac.jp

IntechOpen

References

[1] Gozalvez J. 5G tests and demonstrations [mobile radio]. IEEE Vehicular Technology Magazine. 2015;**10**(2):16-25. DOI: 10.1109/MVT.2015.2414831

[2] Sankapal BR, Gajare HB, Karade SS, Salunkhe RR, Dubal DP. Zinc oxide encapsulated carbon nanotube thin films for energy storage applications. Electrochimica Acta. 2016;**192**:377-384. DOI: 10.1016/j.electacta.2016.01.193

[3] Mallory GO, Hajdu JB. EP: Fundamentals and Applications. New Jersey, USA: William Andrew; 1990. DOI: 10.1002/9783527616770.ch2

[4] Adachi H, Taki K, Nagamine S, Yusa A, Ohshima M. Supercritical carbon dioxide assisted EP on thermoplastic polymers. The Journal of Supercritical Fluids. 2009;**49**(2):265-270. DOI: 10.1016/j.supflu.2013.11.012

[5] Watkins JJ, McCarthy TJ. Polymer/metal nanocomposite synthesis in supercritical CO_2. Chemistry of Materials. 1995;**7**(11):1991-1994. DOI: 10.1021/cm00059a001

[6] Brunner G. Gas Extraction: An Introduction to Fundamentals of Supercritical Fluids and the Application to Separation Processes. New York, USA: Springer Science & Business Media; 2013. DOI: 10.1002/bbpc.19961000668

[7] Clifford A, Clifford T. Fundamentals of Supercritical Fluids. Oxford, UK: Oxford University Press; 1999

[8] Sawan SP, Sawan SP. Supercritical Fluid Cleaning: Fundamentals, Technology and Applications. Amsterdam, Netherlands: Elsevier; 1998

[9] Gorla C, Emanetoglu N, Liang S, Mayo W, Lu Y, Wraback M, et al. Structural, optical, and surface acoustic wave properties of epitaxial zinc oxide films grown on (0112) sapphire by metalorganic chemical vapor deposition. Journal of Applied Physics. 1999;**85**(5):2595-2602. DOI: 10.1063/1.369577

[10] Panigrahy B, Aslam M, Misra D, Bahadur D. Polymer-mediated shape-selective synthesis of zinc oxide nanostructures using a single-step aqueous approach. CrystEngComm. 2009;**11**(9):1920-1925. DOI: 10.1039/B904833M

[11] Ku C-H, Wu J-J. Aqueous solution route to high-aspect-ratio zinc oxide nanostructures on indium tin oxide substrates. The Journal of Physical Chemistry B. 2006;**110**(26):12981-12985. DOI: 10.1021/jp061458b

[12] Zhang Q, Tian C, Wu A, Tan T, Sun L, Wang L, et al. A facile one-pot route for the controllable growth of small sized and well-dispersed zinc oxide particles on GO-derived graphene. Journal of Materials Chemistry. 2012;**22**(23):11778-11784. DOI: 10.1039/C2JM31401K

[13] Peulon S, Lincot D. Mechanistic study of cathodic electrodeposition of zinc oxide and zinc hydroxychloride films from oxygenated aqueous zinc chloride solutions. Journal of the Electrochemical Society. 1998;**145**(3):864-874. DOI: 10.1149/1.1838359

[14] Peulon S, Lincot D. Cathodic electrodeposition from aqueous solution of dense or open-structured zinc oxide films. Advanced Materials. 1996;**8**(2):166-170. DOI: 10.1002/adma.19960080216

[15] Hu C-C, Hsu H-C, Chang K-H. Cathodic deposition of TiO_2: Effects of H_2O_2 and deposition modes. Journal of the Electrochemical Society.

2012;**159**(7):D418-DD24. DOI: 10.1149/2.026207jes

[16] Chang T-FM, Sato T, Sone M. Fabrication of TiO_2 micro-structures by cathodic deposition. Microelectronic Engineering. 2014;**121**:80-82. DOI: 10.1016/j.mee.2014.03.033

[17] Lee HM, Ge M, Sahu B, Tarakeshwar P, Kim KS. Geometrical and electronic structures of gold, silver, and gold–silver binary clusters: Origins of ductility of gold and gold–silver alloy formation. The Journal of Physical Chemistry B. 2003;**107**(37):9994-10005. DOI: 10.1021/jp034826+

[18] Hsiao Y-C, Wu T-F, Wang Y-S, Hu C-C, Huang C. Evaluating the sensitizing effect on the photocatalytic decoloration of dyes using anatase-TiO_2. Applied Catalysis B: Environmental. 2014;**148**:250-257. DOI: 10.1016/j.apcatb.2013.11.014

[19] Nakaoka K, Ueyama J, Ogura K. Photoelectrochemical behavior of electrodeposited CuO and Cu_2O thin films on conducting substrates. Journal of the Electrochemical Society. 2004;**151**(10):C661-C6C5. DOI: 10.1149/1.1789155

[20] Lu X, Wang G, Xie S, Shi J, Li W, Tong Y, et al. Efficient photocatalytic hydrogen evolution over hydrogenated zinc oxide nanorod arrays. Chemical Communications. 2012;**48**(62):7717-7719. DOI: 10.1039/C2CC31773G

[21] Gawad SA, Baraka A, Morsi M, Eltoum MA. Development of electroless Ni–P–Al_2O_3 and Ni–P–TiO_2 composite coatings from alkaline hypophosphite gluconate baths and their properties. International Journal of Electrochemical Science. 2013;**8**:1722-1734

[22] Thiemig D, Bund A. Characterization of electrodeposited Ni–TiO_2 nanocomposite coatings. Surface and Coatings Technology. 2008;**202**(13):2976-2984. DOI: 10.1016/j.surfcoat.2007.10.035

[23] Parida G, Chaira D, Chopkar M, Basu A. Synthesis and characterization of Ni-TiO_2 composite coatings by electro-co-deposition. Surface and Coatings Technology. 2011;**205**(21-22):4871-4879. DOI: 10.1016/j.surfcoat.2011.04.102

[24] Benea L, Danaila E, Celis J-P. Influence of electro-co-deposition parameters on nano-TiO_2 inclusion into nickel matrix and properties characterization of nanocomposite coatings obtained. Materials Science and Engineering: A. 2014;**610**:106-115. DOI: 10.1016/j.msea.2014.05.028

[25] Momenzadeh M, Sanjabi S. The effect of TiO_2 nanoparticle codeposition on microstructure and corrosion resistance of electroless Ni-P coating. Materials and Corrosion. 2012;**63**(7):614-619. DOI: 10.1002/maco.201005985

[26] Esken D, Zhang X, Lebedev OI, Schröder F, Fischer RA. Pd@MOF-5: Limitations of gas-phase infiltration and solution impregnation of $[Zn_4O(bdc)_3]$ (MOF-5) with metal–organic palladium precursors for loading with Pd nanoparticles. Journal of Materials Chemistry. 2009;**19**(9):1314-1319. DOI: 10.1039/B815977G

[27] Wang Y, Zheng H, Li Z, Xie K. Investigation of the interaction between $Cu(acac)_2$ and NH_4Y in the preparation of chlorine-free CuY catalysts for the oxidative carbonylation of methanol to a fuel additive. RSC Advances. 2015;**5**(124):102323-102331. DOI: 10.1039/C5RA19941G

[28] Tang W, Xu K, Wang P, Li X. Surface roughness and resistivity of Au film on Si-(111) substrate. Microelectronic Engineering. 2003;**66**(1-4):445-450. DOI: 10.1016/S0167-9317(02)00909-7

[29] Jiao S, Zhang K, Bai S, Li H, Gao S, Li H, et al. Controlled morphology evolution of zinc oxide nanostructures in the electrochemical deposition: From the point of view of chloride ions. Electrochimica Acta. 2013;**111**:64-70. DOI: 10.1016/j.electacta.2013.08.050

[30] El Hichou A, Stein N, Boulanger C, Johann L. Structural and spectroscopic ellipsometry characterization for electrodeposited zinc oxide growth at different hydrogen peroxide concentration. Thin Solid Films. 2010;**518**(15):4150-4155. DOI: 10.1016/j.tsf.2009.11.070

[31] Lin W-H, Chang T-FM, Lu Y-H, Sato T, Sone M, Wei K-H, et al. Supercritical CO_2-assisted electrochemical deposition of zinc oxide mesocrystals for practical Photoelectrochemical applications. The Journal of Physical Chemistry C. 2013;**117**(48):25596-25603. DOI: 10.1021/jp409607m

[32] Pauporté T, Lincot D. Hydrogen peroxide oxygen precursor for zinc oxide electrodeposition II—Mechanistic aspects. Journal of Electroanalytical Chemistry. 2001;**517**(1):54-62. DOI: 10.1016/S0022-0728(01)00674-X

[33] Bian S-W, Mudunkotuwa IA, Rupasinghe T, Grassian VH. Aggregation and dissolution of 4 nm zinc oxide nanoparticles in aqueous environments: Influence of pH, ionic strength, size, and adsorption of humic acid. Langmuir. 2011;**27**(10):6059-6068. DOI: 10.1021/la200570n

[34] Wippermann K, Schultze J, Kessel R, Penninger J. The inhibition of zinc corrosion by bisaminotriazole and other triazole derivatives. Corrosion Science. 1991;**32**(2):205225-223230. DOI: 10.1016/0010-938X(91)90044-P

[35] Tena-Zaera R, Elias J, Wang G, Lévy-Clément C. Role of chloride ions on electrochemical deposition of zinc oxide nanowire arrays from O_2 reduction. The Journal of Physical Chemistry C. 2007;**111**(45):16706-16711. DOI: 10.1021/jp073985g

[36] Tekerlekopoulou AG, Pavlou S, Vayenas DV. Removal of ammonium, iron and manganese from potable water in biofiltration units: A review. Journal of Chemical Technology and Biotechnology. 2013;**88**(5):751-773. DOI: 10.1002/jctb.4031

[37] Woo B-H, Sone M, Shibata A, Ishiyama C, Masuda K, Yamagata M, et al. Effects of ScCO₂ cat. in metallization on polymer by EP. Surface and Coatings Technology. 2009;**203**(14):1971-1978. DOI: 10.1016/j.surfcoat.2009.01.031

[38] Tengsuwan S, Ohshima M. Electroless nickel plating on polypropylene via hydrophilic modification and supercritical carbon dioxide Pd-complex infusion. The Journal of Supercritical Fluids. 2012;**69**:117-123. DOI: 10.1016/j.supflu.2012.06.002

[39] Sano M, Tahara Y, Chen C-Y, Chang T-FM, Hashimoto T, Kurosu H, et al. Application of supercritical carbon dioxide in cat. and Ni-P EP of nylon 6, 6 fabric. Surface and Coatings Technology. 2016;**302**:336-343. DOI: 10.1016/j.surfcoat.2016.06.037

[40] Ns B, Sakai G, Miura N, Yamazoe N. Preparation of stabilized nanosized tin oxide particles by hydrothermal treatment. Journal of the American Ceramic Society. 2000;**83**(12):2983-2987. DOI: 10.1111/j.1151-2916.2000.tb01670.x

[41] Korotcenkov G, Cho B. The role of the grain size on thermal stability of nanostructured SnO_2 and In_2O_3 metal oxides films aimed for gas sensor application. Progress in Crystal Growth and Characterization of Materials. 2012;**58**:167-208. DOI: 10.1016/j.pcrysgrow.2012.07.001

[42] Abdel Hamid Z, Ghayad IM. Characteristics of electrodeposition of Ni-polyethylene composite coatings. Materials Letters. 2002;**53**(4):238-243. DOI: 10.1016/S0167-577X(01)00484-0

[43] Müller C, Sarret M, Benballa M. ZnNi/SiC composites obtained from an alkaline bath. Surface and Coatings Technology. 2003;**162**(1):49-53. DOI: 10.1016/S0257-8972(02)00360-2

[44] Krishnaveni K, Sankara Narayanan TSN, Seshadri SK. Electrodeposited Ni–B–Si$_3$N$_4$ composite coating: Preparation and evaluation of its characteristic properties. Journal of Alloys and Compounds. 2008;**466**(1):412-420. DOI: 10.1016/j.jallcom.2007.11.104

[45] Liao C-W, Lee H-B, Hou K-H, Jian S-Y, Lu C-E, Ger M-D. Characterization of the Cr-C/Si$_3$N$_4$ composite coatings electroplated from a trivalent chromium bath. Electrochimica Acta. 2016;**209**:244-253. DOI: 10.1016/j.electacta.2016.05.084

[46] Gutzeit G. Industrial nickel coating by chemical catalytic reduction. Anti-Corrosion Methods and Materials. 1956;**3**(6):208. DOI: 10.1108/eb019191

[47] Cavallotti P, Salvago G. Studies on chemical reduction of nickel and cobalt by hypophosphite. Pt. 2. Characteristics of the process. Electrochim Metallorum. 1968;**3**(3):239-266

[48] Salvago G, Cavallotti P. Characteristics of the chemical reduction of nickel alloys with hypophosphite. Plating. 1972;**59**(7):665-671

[49] Rondin JP, Hintermann H. A calorimetric study of the electroless deposition of nickel. Journal of the Electrochemical Society. 1970;**117**(2):160-167. DOI: 10.1149/1.2408405

[50] Mizuhashi S, Cordonier CEJ, Matsui H, Honma H, Takai O. Comparative study on physical and electrochemical characteristics of thin films deposited from electroless platinum plating baths. Thin Solid Films. 2016;**619**(Supplement C): 328-335. DOI: 10.1016/j.tsf.2016.10.040

[51] Mizuhashi S, Cordonier CE, Honma H, Takai O. Stabilization of an electroless platinum plating bath using S-bearing additives. Journal of the Electrochemical Society. 2015;**162**(10):D497-D502. DOI: 10.1149/2.0081510jes

[52] Rao CRK, Pushpavanam M. Electroless deposition of platinum on titanium substrates. Materials Chemistry and Physics. 2001;**68**(1):62-65. DOI: 10.1016/S0254-0584(00)00268-6

[53] Pak JJ, Cha S-E, Ahn H-J, Lee S-K, editors. Fabrication of ionic polymer metal composites by EP of Pt. In: Proc of the 32nd Intl Symp on Robotics. 2001

[54] Zahavi J, Hazan J. Electrodeposited nickel composites containing diamond particles. Plating and Surface Finishing. 1983;**70**(2):57-61

[55] Lee W-H, Tang S-C, Chung K-C. Effects of direct current and pulse-plating on the co-deposition of nickel and nanometer diamond powder. Surface and Coatings Technology. 1999;**120**:607-611. DOI: 10.1016/S0257-8972(99)00445-4